

# Unsupervised Visual Defect Detection with Score-Based Generative Model

Yapeng Teng<sup>1</sup>Haoyang Li<sup>1</sup>Fuzhen Cai<sup>1</sup>Ming Shao<sup>2</sup>Siyu Xia<sup>1</sup><sup>1</sup> Southeast University <sup>2</sup> University of Massachusetts Dartmouth

## Abstract

*Anomaly Detection (AD), as a critical problem, has been widely discussed. In this paper, we specialize in one specific problem, Visual Defect Detection (VDD), in many industrial applications. And in practice, defect image samples are very rare and difficult to collect. Thus, we focus on the unsupervised visual defect detection and localization tasks and propose a novel framework based on the recent score-based generative models, which synthesize the real image by iterative denoising through stochastic differential equations (SDEs). Our work is inspired by the fact that with noise injected into the original image, the defects may be changed into normal cases in the denoising process (i.e., reconstruction). First, based on the assumption that the anomalous data lie in the low probability density region of the normal data distribution, we explain a common phenomenon that occurs when reconstruction-based approaches are applied to VDD: normal pixels also change during the reconstruction process. Second, due to the differences in normal pixels between the reconstructed and original images, a time-dependent gradient value (i.e., score) of normal data distribution is utilized as a metric, rather than reconstruction loss, to gauge the defects. Third, a novel  $T$  scales approach is developed to dramatically reduce the required number of iterations, accelerating the inference process. These practices allow our model to generalize VDD in an unsupervised manner while maintaining reasonably good performance. We evaluate our method on several datasets to demonstrate its effectiveness.*

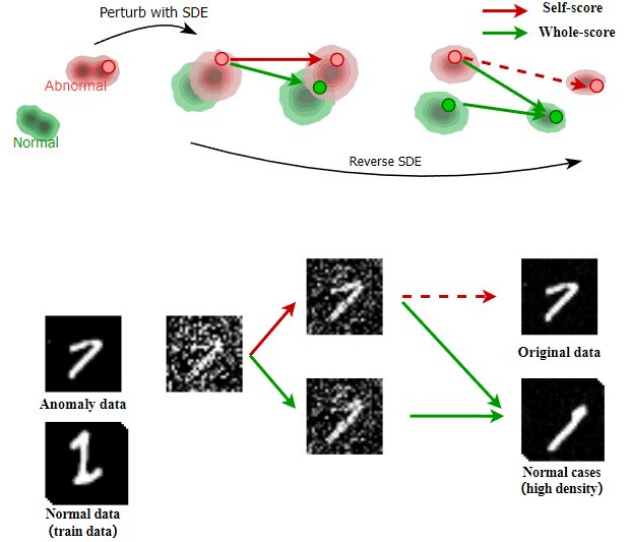


Figure 1. The red and green contour plots depict the distributions of normal and abnormal data, respectively; the red dot represents an abnormal sample, and the green dot represents a being-reconstructed sample that is gradually transforming into normal cases. Given an anomaly data, on the left, the noise is injected to blur it. When the model is iterated through **whole-score**, the defect is recovered into normal modes, as indicated by the green arrow, while through **self-score**, the noise image is restored to the original image, as indicated by the red arrow. Two whole-score values pointing to the normal cases indicate that the upper noise image, whose defect is gradually back to its original, requires a larger **whole-score** value than the lower image, which has been changing defect, to correct the defect.

## 1. Introduction

AD, whose objective is to detect previously unseen rare objects or events, plays key roles in a variety of applications, including industrial manufacturing [5, 16, 19, 28, 50] and medical analysis [26, 36, 37, 40]. VDD issues, a specific sub-problem of AD, which we define in this paper as where the visual variation in the known classes is generally modest, such as unified backgrounds, and defects manifest as localized patches with anomalous visual appearances to prevent ambiguity, have been valued in various industrial prod-

ucts. As anomalous samples are rare in real-world scenarios, this poses challenges, especially for supervised learning models. Alternative solutions through generative models trained only on normal samples in an unsupervised manner have been prevailing recently, including Auto-encoder (AE) [13], Generative Adversarial Network (GAN) [11], Flow [9] and their variants. Nonetheless, difficulty remains in applying these methods to high-dimensional data such as images. For example, AE is known for its blurred reconstructions and indistinguishable defects, and GAN or Flow models need additional overhead in developing encoders or

dedicated dimensionality reduction modules, which is both time- and computational-consuming.

To effectively and directly apply generative models to VDD, we propose **Score-DD**, which is characterized by leveraging the recent score-based generative modeling through SDEs [38] and employing the score (i.e., the gradient of the log probability density with respect to data) instead of conventional reconstruction loss as a metric. Generally, similar to diffusion models [14], score-based generative models gradually convert a pure Gaussian noise vector into a similar realistic training image through iterating an equation containing a score value, which we renamed “**whole-score**” in this paper and can also be used to measure the distance from the high probability density region of the training data. Furthermore, we design another iteration process by **self-score**, which guides samples back to the original. The key idea of Score-DD is shown in Fig. 1. Given a defect image, we first add some noise to it, and then start to stimulate two distinct processes using whole-score and self-score. In detail, with iteration through whole-score, the noise data is gradually brought closer to the high density region of the normal data distribution by the guidance of whole-score; on the other hand, based on the easy-to-meet assumption in the VDD setting that all anomalous data exist in the low density region of the normal data distribution, the noise images obtained by iteration through self-score will gradually reveal defects far from the high density region. The full iterative processes are not required; notably, after getting two noise images in the middle, we can calculate their whole-score values to evaluate their distances from the high density region, and their divergence will be leveraged for defect detection and localization. As shown in the middle of Fig. 1, the upper noise image “7” is further away from the high density region than the lower one.

Our main contribution is to solve three challenges. First, our observations have identified and explained key issues that are common phenomena when reconstruction-based methods are applied to VDD: the reconstructed normal pixels do not exactly match the original image; therefore, a simple pixel-wise comparison between the reconstructed and original data for VDD is not reliable. Second, based on the initial assumption, we propose a new metric through the whole-score, instead of traditional reconstruction loss, to mitigate this issue. Third, the reverse process of score-model is less-efficient for certain setting of hyperparameters, e.g., a larger initial moment  $t$  in our case. Instead of launching a large  $t$ , we propose to investigate a set of smaller parameters, i.e.,  $\{t\}$  with only a few steps in reverse for each. This ensemble strategy allows us to consider different “reconstructed and original” data pairs and enables a more reliable detection mechanism, termed  $T$  scales.

Besides, most existing methods rely on pre-trained networks for feature extraction, external data, extra mecha-

nisms for good performance, or they need to redesign their model structure and loss function. Our goal is to explore the characteristics of the score model applied to unsupervised VDD and provide a simple and effective scheme not dependent on other models or mechanisms. Unlike them, our score model is just trained on normal data in an unsupervised fashion. And it can also easily be extended and combined with other mechanisms because our method does not modify the training procedure of the score-based generative model. We evaluate our method on several datasets to verify its effectiveness. Among them, our method achieves the state-of-the-art (SOTA) **98.24 image-level AUC** and **97.78 pixel-level AUC** on the challenging MVTEC AD dataset [5].

## 2. Related work

In this section, we mainly review previous approaches based on generative models. AE is trained to generate normal data but fails to reconstruct the abnormal samples. However, the output is often blurred [16], or defects are well restored [51] due to the nature of generalization. To fix these problems, recent works have developed and discussed the memory mechanism [10, 16], SSIM Loss [43], Mask strategy [51], denoising autoencoder [17] and forgery defect [50]. However, these methods have recently been superseded by the following competitive generative models.

Recently, GAN and its generative and discriminative networks have been leveraged in AD tasks. In detail, the generative networks learn to map the noise from a latent space to anomaly-free data distribution, while the discriminant network determines whether it comes from anomaly-free data distribution. However, as GAN lacks dedicated encoders to produce hidden variables of the input data, additional efforts are required to develop networks to search for the hidden variables [2, 3, 36].

Another branch of work is based on the approach “normalized flow” which learns and manages to map the distribution of normal data reversely to a simple Gaussian distribution. The distribution of normal data supposes to be close to the center of the Gaussian kernels (i.e., high-density region), while the abnormal data shall exist in the low density region, an indicator for data with defects in the testing phase. However, as the hidden layer dimension must match the data dimension in these methods, when working on data of a larger size, e.g., high-resolution images, the model parameters expand quickly. Therefore, the flow-based methods [12, 31, 32, 49] usually take feature maps extracted by a network pre-trained on a large-scale dataset, e.g., ImageNet.

## 3. Background

### 3.1. Score-based Generative Model for VDD

The unsupervised VDD model discussed in this paper is trained on a normal dataset  $\mathbf{X}_N$  in an unsupervised fashion

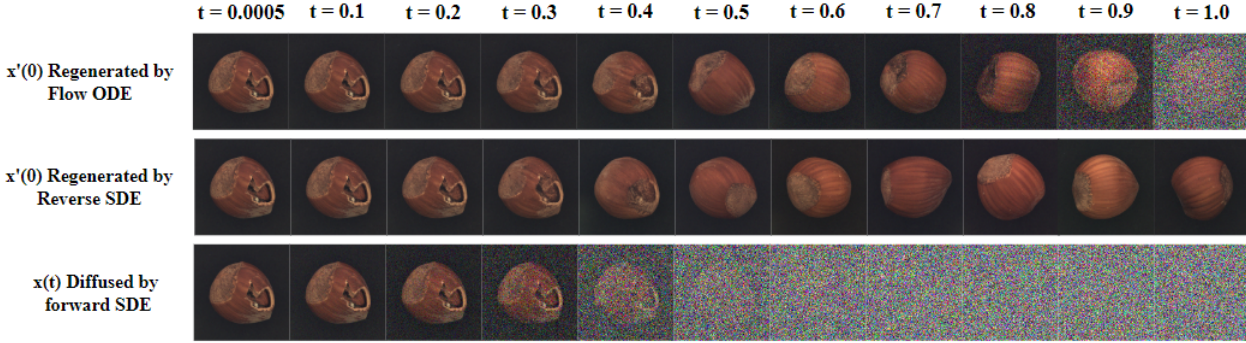


Figure 2. Regenerate samples by solving the probability flow ODE and reverse SDE on  $[0, t]$  with initial point  $\mathbf{x}(t) = \mu(t)\mathbf{x}(0) + \sigma(t)\mathbf{z}(t)$  for  $\mathbf{z}(t) \sim \mathcal{N}(0, \mathbf{I})$  trained on MVTEC AD dataset.

while tested on a blend of a normal and abnormal dataset  $\mathbf{X}_{N+A}$ , where the main objects of the abnormal data contain defect patches. Our framework is inspired by the Denoising AutoEncoder (DAE) [17]. We can extend the DAE by integrating the diffusion process with score-based generative models [24, 48]. In particular, we can model a diffusion process by using forward SDE to inject a certain amount of noise into the data and implement the reverse diffusion process as denoising. Ideally, the defects would be treated as noise and be recovered to normal data. This procedure is shown in Fig. 2. With the reconstructed data gained from the reverse diffusion, we are able to compare it with the original data through certain metrics to detect defects. We will briefly introduce: (1) diffusion process; (2) reverse process; (3) the probability flow ODE; (4) whole-score and self-score .

**Diffusion process.** Diffusion process gradually adds noise to the original data  $\mathbf{x}$  through forward SDE [38], and yields a sequence  $\{\mathbf{x}(t)\}$  through:

$$d\mathbf{x}(t) = f(t)\mathbf{x}(t)dt + g(t)d\mathbf{w}(t), \quad (1)$$

where  $t \in [0, 1]$  indicates the time stamp,  $\mathbf{w}(t)$  denotes a standard Wiener process, and the drift coefficient  $f(t)$  and the diffusion coefficient  $g(t)$  are fixed. Therefore, it is essentially an ordinary differential equation (ODE) driven by the noise. We can interpret  $d\mathbf{w}(t)$  as an infinitesimal Gaussian noise. The solution to this diffusion process in Eq. (1) is  $\{\mathbf{x}(t)\}_{t \in [0, 1]}$ . Assume  $p_t(\mathbf{x})$  denotes the probability density of solution and  $p_{0t}(\mathbf{x}(t)|\mathbf{x}(0))$  denotes the transition distribution from  $\mathbf{x}(0)$  to  $\mathbf{x}(t)$ . By definition,  $p_{data}(\mathbf{x}) \approx p_0(\mathbf{x})$ . Based on Eq. (1), we can continuously add noises to the original data  $\mathbf{x}(0) \sim p_0(\mathbf{x})$ . This process gradually removes details and structure of the data as  $t$  increases, and the distribution of noise data  $p_1(\mathbf{x})$  satisfies a tractable prior distribution  $\pi(\mathbf{x})$ .

**Reverse process.** Diffusion process starts from  $\mathbf{x}(0)$  and ends up with  $\mathbf{x}(t)$ . The reverse process aims to recover the original data from  $\mathbf{x}(t)$  and get an similar value,  $\mathbf{x}'(0)$ , gen-

erated by the reverse of a diffusion process of Eq. (1), which is also a diffusion process and can be achieved by:

$$d\mathbf{x}(t) = (f(t)\mathbf{x}(t) - g(t)^2 \nabla_{\mathbf{x}} \log p_t(\mathbf{x}(t)))d\bar{t} + g(t)d\bar{\mathbf{w}}(t), \quad (2)$$

where  $d\bar{t}$  represents negative time step,  $\bar{\mathbf{w}}$  denotes a standard Wiener process in the reversal time direction. Therefore, the objective of score-based generative model transforms to learn the score function  $\nabla_{\mathbf{x}} \log p_t(\mathbf{x}(t))$  in Eq. (2). We can estimate  $\nabla_{\mathbf{x}} \log p_t(\mathbf{x})$  by training a score-based model  $s_\theta(\mathbf{x}(t), t)$  on training dataset  $\mathbf{X}_N$ , where  $s_\theta(\mathbf{x}(t), t)$  adopts a variant of U-net that requires both  $\mathbf{x}(t)$  and  $t$  inputs. The goal now is to minimize the following loss [41]:

$$\mathcal{L}(\theta; \lambda(\cdot)) := \frac{1}{2} \int_0^1 \mathbb{E}_{p_0(\mathbf{x})p_{0t}(\mathbf{x}(t)|\mathbf{x}(0))} [\lambda(t)] \|\nabla_{\mathbf{x}} \log p_{0t}(\mathbf{x}(t)|\mathbf{x}(0)) - s_\theta(\mathbf{x}(t), t)\|_2^2 dt, \quad (3)$$

which is equivalent to a constant that is irrelevant to  $\theta$ . Additionally, if the drift coefficient  $f(t)$  is linear, the  $p_{0t}(\mathbf{x}(t)|\mathbf{x}(0)) = \mathcal{N}(\mathbf{x}(t); \mu(t)\mathbf{x}(0), \sigma^2(t)\mathbf{I})$  will be a tractable Gaussian distribution, and

$$\mathbf{x}(t) = \mu(t)\mathbf{x}(0) + \sigma(t)\mathbf{z}(t), \quad (4)$$

where  $\mathbf{z}(t) \sim \mathcal{N}(0, \mathbf{I})$ . Fortunately Variance Exploding (VE), Variance Preserving (VP) and sub-VP SDE introduced in [38] satisfy the linear drift coefficient condition (check more details in Appendix A.3), and therefore,  $\nabla_{\mathbf{x}} \log p_{0t}(\mathbf{x}(t)|\mathbf{x}(0)) = -\frac{\mathbf{z}(t)}{\sigma(t)}$  of each sample can be solved. Following this, we are able to train a score-based model  $s_\theta(\mathbf{x}(t), t)$  by sampling  $\mathbf{x}(0) \sim p_0(\mathbf{x})$  from training dataset, uniformly and randomly sampling  $t$  in  $[0, 1]$ , and getting  $\mathbf{x}(t) \sim p_{0t}(\mathbf{x}(t)|\mathbf{x}(0))$ .

**Probability flow ODE.** In addition to the Eq. (2), there is an alternative solution to the reverse diffusion process termed probability flow ODE [23, 38], abbreviated as Flow ODE. The Flow ODE shares the same marginal distribution

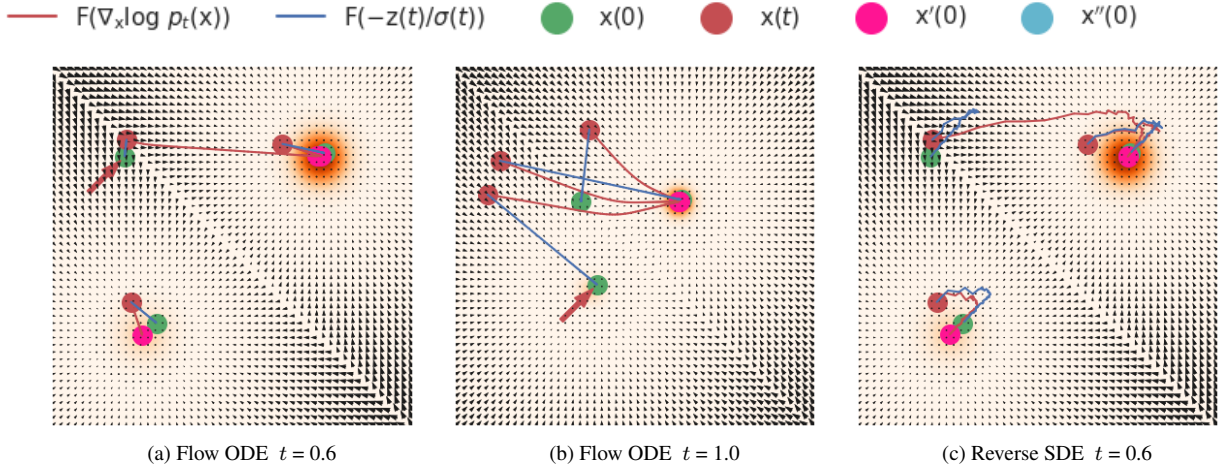


Figure 3. Exploratory experiment based on the VE SDE.  $p_{data}(\mathbf{x})$  is shown in an orange colormap. The red trajectory represents the reverse diffusion process from  $\mathbf{x}(t)$  to  $\mathbf{x}'(0)$  driven by  $\nabla_{\mathbf{x}} \log p_t(\mathbf{x}(t))$ , and the blue trajectory is the process from  $\mathbf{x}(t)$  to  $\mathbf{x}''(0)$  driven by  $-\mathbf{z}(t)/\sigma(t)$ . (a) Iterating the Flow ODE with  $t = 0.6$ . (b) Iterating the Flow ODE with  $t = 1.0$ . (c) Iterating the Reverse SDE with  $t = 0.6$ . With arrows, we label the abnormal data  $\mathbf{x}(0)$  in (a), and the normal data  $\mathbf{x}(0)$  in (b) whose corresponding  $\mathbf{x}'(0)$  eventually moves to other high-density region.

$p_t(\mathbf{x})$  with SDE of Eq. (1) and can be defined as:

$$d\mathbf{x}(t) = (f(t)\mathbf{x}(t) - \frac{1}{2}g(t)^2\nabla_{\mathbf{x}} \log p_t(\mathbf{x}(t)))dt. \quad (5)$$

In particular, the Flow ODE does not include random terms but retains the same score function  $\nabla_{\mathbf{x}} \log p_t(\mathbf{x}(t))$ . Therefore, we can also plug  $s_{\theta}(\mathbf{x}(t), t)$  into Eq. (2) or Eq. (5) to generate samples.

**Whole-score and self-score.** It can be seen that the output of the trained score model  $s_{\theta}(\mathbf{x}, t) \approx \nabla_{\mathbf{x}} \log p_t(\mathbf{x}(t))$  is the gradient pointing to the high-density regions of  $\mathbf{X}_N$ , and plays a key role in the reverse process. Therefore, we term it as **whole-score**  $s_w(\mathbf{x}, t)$ . In addition, we use score  $s_e(\mathbf{x}, t) = -\frac{\mathbf{z}(t)}{\sigma(t)}$  relatively to each sample denoted as **self-score**. Both whole- and self-score will be discussed and used in our proposed Score-DD model.

### 3.2. Issues and Observations

We regenerate a series of images as shown in Fig. 2. In particular, given a test image, with predetermined  $t \in (0, 1]$ , we inject noise into  $\mathbf{x}(0)$  according to the forward SDEs to achieve  $\mathbf{x}(t)$ . Simulating reverse process by reverse SDE or Flow ODE, we are allowed to reconstruct images  $\mathbf{x}'(0)$ . Note that with different  $t \in \{0.0005, 0.1, \dots\}$ , details and structures are gradually removed from left to right in the third row of Fig. 2. Based on the difference between the original and reconstructed images, we can localize the defects. For example, if using the reconstruction of  $t = 0.5$  in the first row of Fig. 2, we may easily locate the defects. However, picking an appropriate value of  $t$  is not trivial.

When using a smaller  $t$ , not all defects can be well changed into the normal mode. On the other hand, when using a larger  $t$ , the normal pixels in the reconstructed image are slightly different from the original image in pixel space.

To provide more insights behind these phenomena, we conduct another experiment in Fig. 3 to explore how the score-based model transforms anomalous data into a normal pattern and the reasons for deterioration in normal regions of the original images. For demonstration purposes, we consider VE SDE where  $d\mathbf{x}(t) = \sqrt{\frac{d[\sigma^2(t)]}{dt}}d\mathbf{w}(t)$ . Assume that the distribution of positive data is  $\frac{1}{5}\mathcal{N}((-5, -5), \mathbf{I}) + \frac{4}{5}\mathcal{N}((5, 5), \mathbf{I})$ , and set 100 time steps in  $[0, 1]$ . Other details are presented in Appendix B. Following the steps discussed above, we set the initial diffusion time step  $t$  and obtain  $\mathbf{x}(t)$  by Eq. (4), and then conduct the reverse process through Flow ODE in Eq. (5) or reverse SDE in Eq. (2). In Fig. 3, anomalous data points originally located in low probability density move to high probability density regions driven by whole-score  $s_w(\mathbf{x}, t)$  and end up as  $\mathbf{x}'(0)$ . For normal data, as shown in Fig. 3a and Fig. 3c, with a suitable value of  $t$ , e.g.,  $t = 0.6$ , the deviation of the  $\mathbf{x}'(0)$  from  $\mathbf{x}(0)$  is smaller. When  $t = 1.0$ , some normal data marked by arrows in Fig. 3b has trouble returning to the vicinity of  $\mathbf{x}(0)$ . The primary reason is that  $s_w(\mathbf{x}, t)$  is learned to enforces the  $\mathbf{x}'(0)$  moving towards the high probability density region of training data. When  $t = 1.0$ , mixed Gaussians are fused into a tractable Gaussian distribution  $p_1(\mathbf{x}) \approx \pi(\mathbf{x})$ . Therefore, some normal data are driven into the other Gaussian cores, which deviate significantly from  $\mathbf{x}(0)$ .

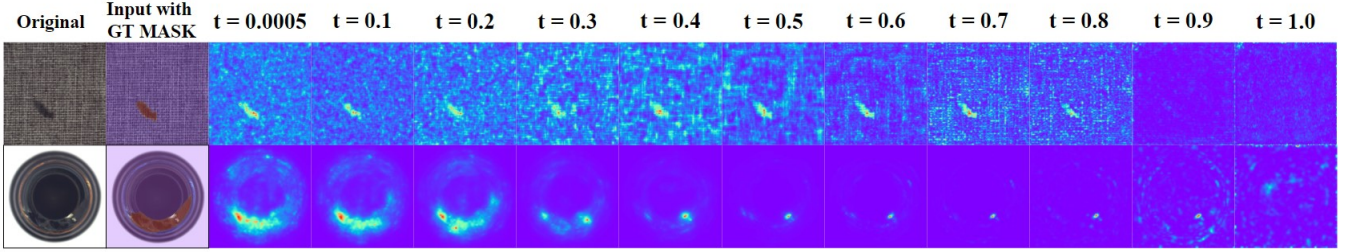


Figure 4. Different semantic information of score model at different moments. Set different initial time  $t$ , iterate  $r = 1$  steps with the Flow ODE, and present upsampling  $64 \times 64$  feature map of score model.

## 4. Proposed Method

### 4.1. Leveraging Whole-scores to Localize Defects

One of the major characters identified in Fig. 3 is that the whole-score drives the noise data towards the high density regions, which makes anomalous data, originally located in the low density region, eventually falls into the high density regions; unexpectedly, this also makes it difficult to return to the vicinity of the original data for some normal data. Thus, we shall carefully select  $t$  value to retain the overall contour of the distribution, such that the reconstructed normal data remain in the vicinity of the original data after iterations. Otherwise, the normal region of the original data will be changed significantly, as shown in Fig. 2 when  $t > 0.5$ . This stringent requirement on  $t$  makes comparing the difference between the reconstructed and original image in pixel space a less feasible or reliable solution. However, we find that normal and abnormal data behave differently in the dimension of probability density. From Fig. 3, after sufficient iterations, all normal or abnormal data eventually fall into the high density portion of the normal data distribution. Based on the assumption that original anomaly data is in the low probability density zone and normal data is originally in the high density region, we propose that employing a metric connected to the probability density of normal data, e.g., whole-score  $s_w(\cdot, t) \approx \nabla_{\mathbf{x}} \log p_t(\mathbf{x}(t))$ , is effective for VDD. As a result, we can feed  $\mathbf{x}'(0)$  and  $\mathbf{x}(0)$  into score model to assess their whole-score difference.

### 4.2. Enhancement through Feature Maps

As the score-based model is usually implemented through neural networks, the characteristics of scores can also be reflected by feature maps. Feature maps in deep layers contain more semantic information, while shallow layers are capable of identifying fine-grained information such as lines and colors. Previous works have already investigated the usefulness of feature maps in different network layers for unsupervised AD or VDD [42, 46, 47] as well as semantic segmentation [4] through the middle layers of a score-based model. Therefore, we also adopt the multi-scale feature maps to strengthen the performance through

the U-net architecture as the following.

To avoid using more models, we adopt a similar scheme to process feature maps in [46]. Firstly, calculate the Euclidean distance between the two feature maps after performing  $l_2$  normalization on each feature map. Then, feature maps of the same resolution are summed up, and all feature maps are scaled up to the same resolution by using the “bilinear” interpolations. The products of all feature maps are taken as the output. In our practice, however, we found that the  $l_2$  normalization compromised the feature maps’ efficacy and their visual effects. We believe the reason is that feature maps in a score-based model are not particularly trained for VDD in an supervised manner as in [46]. However, without normalization, feature maps of the same resolution may have different magnitudes. When they are added together, the output will favor the feature maps with greater magnitude, leading to poor results. Therefore, we skip both  $l_2$  normalization and the sum of feature maps of the same resolution. Instead, after we directly calculate the Euclidean distance, feature maps with significant visual effects are selected, and their point-wise products will be used as outputs, as shown in Fig. 5.

### 4.3. $T$ Scales

Another issue identified in practice is the time spent in the reverse process given a large  $t$  value. It takes many iterations with score model to return to  $\mathbf{x}'(0)$ . We are considering whether we can leverage the feature maps of the score model at different moments without the full iteration since the goal is to detect defects rather than generate images.

It has been discussed that the score-based model provides semantics at different moments  $t$  [4], as shown in Fig. 4. Because the feature maps are changing gradually, there may be a lot of redundant information in the feature maps at adjacent moments. Therefore, we are motivated to not perform a full iteration to get the final image, but to iterate just  $r$  steps ( $r$  is a very small integer), and then compute the difference of  $s_w(\cdot, t_r)$  between  $\mathbf{x}'(t_r)$  and  $\mathbf{x}''(t_r)$  to be the representative semantic information in a certain time period around  $t$ , where  $\mathbf{x}''(t)$  represents the true trajectory from  $\mathbf{x}(t)$  to  $\mathbf{x}(0)$ . In order to leverage different informa-

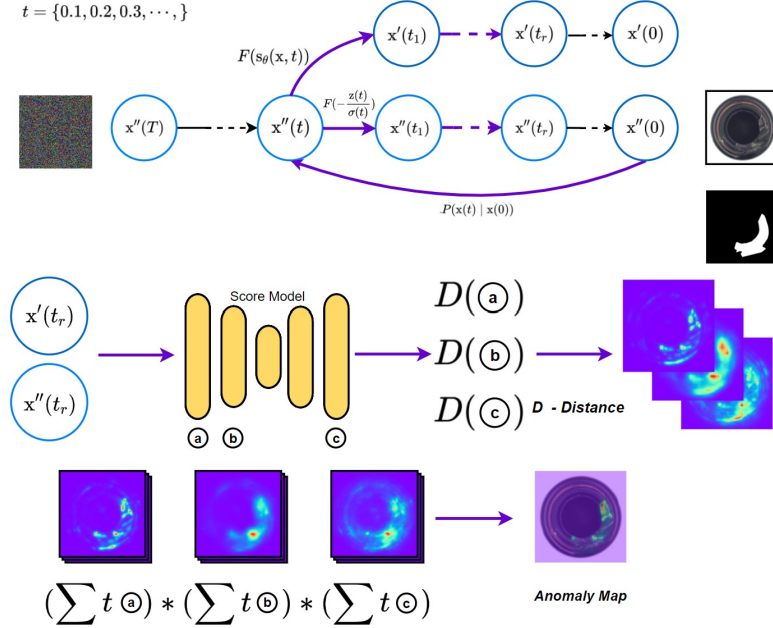


Figure 5. An overview of **Score-DD** for VDD. Set  $\{t\}$  and in each moment  $t$  case, first inject noise to a test image through  $p_{0t}(x(t)|x(0))$  Eq. (4). Then solving Eq. (2) or Eq. (5) by plugging  $s_w(x, t)$  and  $s_e(x, t)$  separately into them. After iterating  $r$  steps, input two samples into score model to extract feature maps. Add up all feature maps of the same resolution at different  $\{t\}$ , then after upsampling, the final anomaly map is obtained by multiplying them up.

tion at different moments, we can apply a set of different moments  $\{t\}$  of capacity  $T$ , and in each  $t$  case, we do the same process as above. We term this approach as  $T$  **scales**, because it will yield  $T$  feature maps to be assembled for anomaly map, as shown in Fig. 5.

Assume that at step  $t$ , we will examine  $x$  at  $t_1 > \dots > t_i > \dots > t_r$  in a sequential manner, where  $t_i - t_{i+1} = \Delta t$  will be used as the approximation of  $dt$  in ODE. Without loss of generality, we elaborate the process of computing  $x'(t_i)$  and  $x''(t_i)$  in each  $t$  case as follows. First, we can achieve  $x'(t_i)$  by replacing  $\nabla_x \log p_t(x(t))$  in Eq. (2) or Eq. (5) with whole-score  $s_w(\cdot, t)$  to build the reverse path as the red path in Fig. 3. Second, we can model  $x''(t_i)$  in adjacent steps by replacing the  $\nabla_x \log p_t(x(t))$  in Eq. (2) or Eq. (5) with self-score  $s_e(\cdot, t)$  as the true trajectory from  $x(t)$  to  $x(0)$ . (The proof process can be found in Appendix A.1). Therefore, if we know self-score  $s_e(\cdot, t)$  relative to  $x(0)$  at each moment, we can approach the original  $x(0)$  from  $x(t)$ , as the blue path in Fig. 3. We elaborate the overall framework of our algorithm in Fig. 5. Specific calculation processes and pseudo-code are given in Appendix A.2.

## 5. Experiment

### 5.1. Datasets

We conducted tests on common benchmarks to validate the effectiveness of our proposed approach, Score-

DD. We describe in detail the data sets used. **MVTec AD dataset** [5] contains 5354 high-resolution images, which is specifically utilized in the unsupervised VDD task. It contains 10 objects and 5 texture categories, and each category contains 60-320 training samples and about 100 test samples. **BeanTech AD dataset** [25] is an industrial dataset containing 2540 high-resolution images of three products. **MNIST** [18] contains 60k training and 10k test  $28 \times 28$  gray-scale handwritten digit images.

### 5.2. Experiment setup

All of the images in the aforementioned dataset are resized to  $256 \times 256$  pixels, except for MNIST which is resized to  $32 \times 32$  pixels. We train a score-based model based on NCSN++ and set 2000 diffusion timesteps for MVTEC AD and BTAD, and we train a score model based on DDPM++ and set 1000 timesteps for MNIST. We use the area under the receiver operating characteristic curve (AUROC) the evaluation metric for both defect detection and localization. In the inference stage, after getting the anomaly map, we leverage it to evaluate the AUROC metric for the location task and the maximum value of each anomaly map to evaluate the AUROC metric for the detection task. Other experiment details are presented in Appendix B.

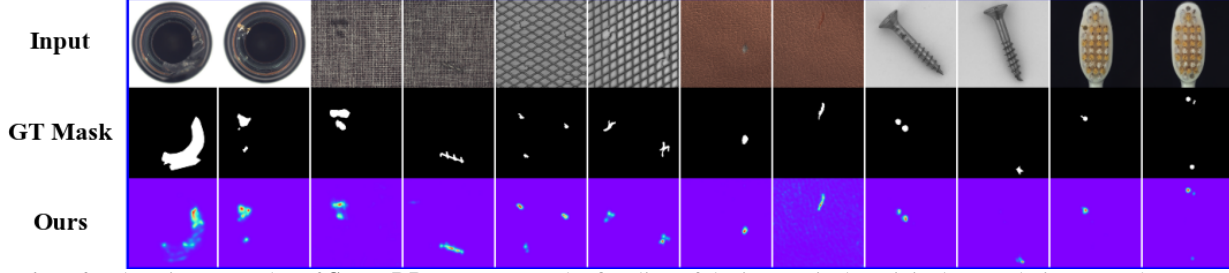


Figure 6. Defect location examples of **Score-DD** on MVTec. The first line of the images is the original anomaly images. The second line is GT MASK. The third line is anomaly map from Score-DD.

Method	RIAD	OCR-GAN	CFlow*	FastFlow*	PaDiM*	PatchCore*	CutPaste	DR/EM	Ours <sup>i</sup>	Ours <sup>ii</sup>	Ours <sup>iii</sup>
carpet	84.2/96.3	99.4/-	<b>100/99.3</b>	<b>100/99.4</b>	-/99.1	98.7/98.9	93.9/98.3	97.0/95.5	96.9/98.9	86.0/95.5	93.0/98.0
grid	99.6/98.8	99.6/-	97.6/99.0	99.7/98.3	-/97.3	98.2/98.7	<b>100/97.5</b>	99.9/ <b>99.7</b>	<b>100/99.7</b>	100/99.6	100/99.5
leather	<b>100/99.4</b>	97.1/-	97.7/ <b>99.7</b>	<b>100/99.5</b>	-/99.2	<b>100/99.3</b>	<b>100/99.5</b>	<b>100/98.6</b>	99.6/99.3	97.8/97.9	98.3/99.0
tile	98.7/89.1	95.5/-	<b>98.7/98.0</b>	<b>100/96.3</b>	-/94.1	98.7/95.6	94.6/90.5	<b>99.6/99.2</b>	98.6/94.4	98.7/95.7	100/94.8
wood	93.0/85.8	95.7/-	<b>99.6/96.7</b>	<b>100/97.0</b>	-/94.9	99.2/95.0	99.1/95.5	99.1/ <b>96.4</b>	98.8/95.1	98.9/96.9	96.2/95.5
bottle	99.9/98.4	99.6/-	<b>100/99.0</b>	<b>100/97.7</b>	-/98.3	<b>100/98.6</b>	98.2/97.6	99.2/ <b>99.1</b>	<b>100/97.9</b>	<b>100/98.1</b>	99.7/95.7
cable	81.9/84.2	99.1/-	<b>100/97.6</b>	<b>100/98.4</b>	-/96.7	99.5/ <b>98.4</b>	81.2/90.0	91.8/94.7	96.8/97.5	95.7/95.1	98.0/97.9
capsule	88.4/92.8	96.2/-	<b>99.3/99.0</b>	<b>100/99.1</b>	-/98.5	98.1/98.8	98.2/97.4	98.5/94.3	96.1/98.6	91.5/97.4	93.2/97.7
hazelnut	83.3/96.1	98.5/-	96.8/98.9	<b>100/99.1</b>	-/98.2	<b>100/98.7</b>	98.3/97.3	<b>100/99.7</b>	99.9/99.2	98.4/ <b>99.4</b>	97.6/99.0
metal Nut	88.5/92.5	99.5/-	91.9/ <b>98.6</b>	<b>100/98.5</b>	-/97.2	<b>100/98.4</b>	99.9/93.1	98.7/ <b>99.5</b>	97.2/97.9	98.9/98.0	99.1/94.7
pill	83.8/95.7	98.3/-	<b>99.9/99.0</b>	<b>99.4/99.2</b>	-/95.7	96.7/97.1	94.9/95.7	98.9/97.6	95.3/96.0	88.3/96.4	93.7/94.4
screw	84.5/98.8	<b>100/-</b>	<b>99.7/98.9</b>	97.8/99.4	-/98.5	98.1/99.4	88.7/96.7	93.9/97.6	99.6/ <b>99.6</b>	98.3/99.8	99.1/99.8
toothbrush	<b>100/98.9</b>	98.7/-	95.2/ <b>99.0</b>	94.4/ <b>98.9</b>	-/98.8	<b>100/98.7</b>	99.4/98.1	<b>100/98.1</b>	99.8/98.3	98.3/97.8	98.9/97.9
transistor	90.9/87.7	98.3/-	99.1/ <b>98.0</b>	<b>99.8/97.3</b>	-/97.5	<b>100/96.3</b>	96.1/93.0	93.1/90.9	95.4/95.2	95.4/94.2	96.4/94.7
zipper	98.1/97.8	99.0/-	98.5/99.1	99.5/98.7	-/98.5	98.8/98.8	<b>99.9/99.3</b>	<b>100/98.8</b>	99.8/ <b>99.3</b>	<b>99.9/99.3</b>	<b>99.9/99.2</b>
Average	91.7/94.2	98.3/-	98.3/ <b>98.6</b>	<b>99.4/98.5</b>	97.9/97.5	<b>99.1/98.1</b>	96.1/96.0	98.0/97.3	98.2/ <b>97.8</b>	96.4/97.4	97.5/97.2

Table 1. Defect detection (**left**) and localization (**right**) performance on the MVTec AD dataset. Methods achieved for the top two AUROC (%) are highlighted in bold. \* means the method is based on a pre-trained model. <sup>i</sup> means Score-DD based on VE SDE; <sup>ii</sup> means Score-DD based on VP SDE; <sup>iii</sup> means Score-DD based on sub-VP SDE.

### 5.3. State-of-the-Art Comparison

**Results on MVTec AD** are shown in Tab. 1, where **Score-DD** based on VE SDE and Flow ODE sampling method achieves SOTA **98.2 image-level AUC** and **97.8 pixel-level AUC**, Score-DD based on VP SDE and reverse SDE sampling method achieves 96.4 image-level AUC and 97.4 pixel-level AUC, and Score-DD based on sub-VP SDE and the Flow ODE sampling method achieves 97.5 image-level AUC and 97.2 pixel-level AUC. We compare our results with the those of SOTA unsupervised VDD methods on the MVTec AD dataset. Specifically, Score-DD outperforms the AE-based method, RIAD [51], and is only 0.1% ↓ than the GAN combined with pseudo-defects method, OCR-GAN [22]. Although our approach still lags behind CFlow [12] and FastFlow [49], works combined Flow with pre-trained models, as well as some others based on pre-trained models, like PatchCore [30], Score-DD does not depend on pre-trained models that contain rich semantic information and have some comparability in some classes. For the methods of creating pseudo-defects to transform unsupervised learning into supervised learning, Score-DD also outperform CutPaste [19], while DR/EM [50], which

uses additional data to create defects and specifically designed reconstruction model and anomaly segmentation model for VDD, achieved SOTA results, Score-DD also outperforms it by 0.2% ↑ in the detection task and 0.5% ↑ in the localization task.

Class	Panda*	PaDiM*	FastFlow*	VT-ADL	OURS
1	96.4/96.4	99.4/97.2	-/95	-/99	99.2/97.7
2	81.0/94.1	79.5/95.2	-/96	-/94	81.1/95.2
3	69.8/98.0	99.4/98.7	-/99	-/77	99.1/98.3
Mean	82.4/96.2	92.7/97.0	-/97	-/79	93.1/97.1

Table 2. Defect detection (**left**) and localization (**right**) performance on BTAD dataset.

**Results on BeanTech AD** are shown in Tab. 2, where Score-DD based on VP SDE and the Flow ODE achieves **93.4 image-level AUC** and **97.1 pixel-level AUC**. Ours outperforms the reconstruction-based method depended on the transformation model, VT-ADL [25]. And compared with the methods relied on pre-trained models, including Panda [29], PaDiM [8], and FastFlow [49], we achieve new SOTA results.

**Results on MNIST** are displayed in Tab. 3. We want

Method	ARAE	OCSVM	AnoGAN	DSVDD	CapsNet <sub>pp</sub>
AUROC	97.5	96.0	91.4	94.8	97.7
Method	OCGAN	LSA	U-Std*	MKDAD*	OURS
AUROC	97.5	97.5	99.35	98.71	95.44

Table 3. Quantitative results of AUROC on the MNIST dataset

to value Score-DD performance on a large dataset, which achieves a **95.44 image-level AUC**. Compared with the methods relied on pre-trained models, U-Std [6] and MKDAD [35], we are about 3.91% ↓ below the best result. More fairly, compared with unsupervised methods, including ARAE [34], OCSVM [7], AnoGAN [20], DSVDD [33], CapsNet<sub>pp</sub> [21], OCGAN [27] and LSA [1]. We come in 2.3% ↓ below the top score.

Case	Reconstruction Loss	Score-DD (w/o $T$ scales)	Score-DD (w/ $T$ scales)
AUROC	84.85 / 89.34	91.30 / 96.24	98.24 / 97.78

Table 4. Quantitative results for ablation studies on MVTEC AD.

#### 5.4. Ablation study and analysis

We do comparative experiments to confirm the efficacy of submodules. Specifically, we run a continuous version experiment (Score-DD without  $T$  scales), iterating from the maximum moment in  $\{t\}$  to near the smallest moment  $\epsilon$ , and then calculate difference of the  $s_w(\cdot, \epsilon)$  and its feature map, to simulate score difference,  $\|\nabla_{\mathbf{x}'} \log p_t(\mathbf{x}'(\epsilon)) - \nabla_{\mathbf{x}''} \log p_t(\mathbf{x}''(\epsilon))\|^2$ , and also do a experiment based on reconstruction loss between  $\mathbf{x}'(0)$  and  $\mathbf{x}''(0)$  as a metric for VDD,  $\|\mathbf{x}'(0) - \mathbf{x}''(0)\|^2$ . When comparing the case with reconstruction loss to Score-DD without  $T$  scales in the Tab. 4, it is clear that the score as a metric is more useful for VDD. Furthermore, when compared to the case without  $T$  scales,  $T$  scales technique can improve performance. This is because it iterates just a few steps, some normal pixels have little opportunity to access other high probability density regions, alleviating the problems discussed above in Sec. 3.2 further, while it also leverages different semantic information at different moments.

#### 5.5. Computational complexity

We propose  $T$  scales technique to speed up the inference process. Take an example from the real case in the MVTEC AD dataset. After we train a score model that needs  $S = 2000$  iteration steps to generate images, we set initial timesteps as  $t = 250/2000$ ; Thus, the inference-time efficiency of Score-DD without  $T$  scales is  $O(t * S - 1 + 2) = O(251)$ . However, with  $T$  scales, we develop a set containing different timesteps  $\{t\}$ . For example, we can take a  $t$  from 250 to 50 every 50 steps,  $\{t\} = \{250, 200, 150, 100, 50\}/2000$  containing  $T = 5$

different timesteps. Therefore, the minimal inference-time efficiency is  $O(T * (r + 2)) = O(T * 3) = O(15)$ , which is more efficient than AnoDDPM [45] whose inference-time efficiency is  $O(t * S) = O(250)$ . The inference time efficiency we calculate is based on the number of runs of the neural network. What’s more,  $T$  scales technique also makes the sequential iteration split into parallel cases, and each  $t$  case needs to iterate just a few  $r$  steps. Therefore, it can also run in parallel to speed things up even further. Moreover, the community is also exploring some ways to accelerate the score model and diffusion model.

#### 5.6. Limitation and future work

Because our work is based on the assumption that data located in the low density region of the normal data distribution are considered abnormal, our work is restricted to the unsupervised VDD setting, and does not win comparative edges in some AD settings. We think part of the reason is that in the AD setting, some changes that are significantly different from the training data, such as changes in the complex background, are of more interest to the model than information about the categories and objects. So it is better to have additional category information or classifiers for the auxiliary [44]. Besides, our approach is sensitive to feature maps that are fixedly selected and cannot be adaptively adjusted according to different images. Thus, difficulties are encountered in experimentally tuning a large dataset like MNIST, resulting in some performance degradation. However, because the training process and loss function don’t change, this can be alleviated by easily extending our method with a professional and generalized classification or segmentation network with self-supervised (e.g., pseudo-defects) or semi-supervised (i.e., several available abnormal samples with image or pixel labels) methods. Since the purpose of this paper is to explore unsupervised solutions that are applicable to the score model and do not depend on other models or mechanisms, we leave this work for the future.

### 6. Conclusion

We propose to use a score-based generative model for unsupervised VDD. Our research indicates that employing a metric for VDD that is linked to the probability density of normal data, e.g., a score value, can efficiently handle the challenge of reconstructed images that differ from the original images with normal pixels in pixel space. In addition, we propose to use  $T$  scales to solve the problem of slow speed due to the need of iterating multiple steps, and since we only need to iterate a few steps at each  $t$  moment, it doesn’t deviate the normal pixels too much from the original data, which in turn improves the accuracy. Without using additional data, algorithms, and models, we have achieved competitive performance on several datasets.

## References

- [1] Davide Abati, Angelo Porrello, Simone Calderara, and Rita Cucchiara. Latent space autoregression for novelty detection. In *Proceedings of the IEEE/CVF Conference on Computer Vision and Pattern Recognition (CVPR)*, June 2019. 8
- [2] Samet Akcay, Amir Atapour-Abarghouei, and Toby P Breckon. Ganomaly: Semi-supervised anomaly detection via adversarial training. In *Asian conference on computer vision*, pages 622–637. Springer, 2018. 2
- [3] Samet Akçay, Amir Atapour-Abarghouei, and Toby P Breckon. Skip-ganomaly: Skip connected and adversarially trained encoder-decoder anomaly detection. In *2019 International Joint Conference on Neural Networks (IJCNN)*, pages 1–8. IEEE, 2019. 2
- [4] Dmitry Baranchuk, Ivan Rubachev, Andrey Voynov, Valentin Khruikov, and Artem Babenko. Label-efficient semantic segmentation with diffusion models. 2022. 5
- [5] Paul Bergmann, Michael Fauser, David Sattlegger, and Carsten Steger. Mvtec ad — a comprehensive real-world dataset for unsupervised anomaly detection. *computer vision and pattern recognition*, 2019. 1, 2, 6
- [6] Paul Bergmann, Michael Fauser, David Sattlegger, and Carsten Steger. Uninformed students: Student-teacher anomaly detection with discriminative latent embeddings. In *Proceedings of the IEEE/CVF Conference on Computer Vision and Pattern Recognition (CVPR)*, June 2020. 8
- [7] Yunqiang Chen, Xiang Sean Zhou, and T.S. Huang. One-class svm for learning in image retrieval. In *Proceedings 2001 International Conference on Image Processing (Cat. No.01CH37205)*, volume 1, pages 34–37 vol.1, 2001. 8
- [8] Thomas Defard, Aleksandr Setkov, Angélique Loesch, and Romaric Audigier. Padim: a patch distribution modeling framework for anomaly detection and localization. In *International Conference on Pattern Recognition*, pages 475–489. Springer, 2021. 7
- [9] Laurent Dinh, Jascha Sohl-Dickstein, and Samy Bengio. Density estimation using real nvp. *arXiv preprint arXiv:1605.08803*, 2016. 1
- [10] Dong Gong, Lingqiao Liu, Vuong Le, Budhaditya Saha, Moussa Reda Mansour, Svetha Venkatesh, and Anton van den Hengel. Memorizing normality to detect anomaly: Memory-augmented deep autoencoder for unsupervised anomaly detection. In *Proceedings of the IEEE/CVF International Conference on Computer Vision*, pages 1705–1714, 2019. 2
- [11] Ian Goodfellow, Jean Pouget-Abadie, Mehdi Mirza, Bing Xu, David Warde-Farley, Sherjil Ozair, Aaron Courville, and Yoshua Bengio. Generative adversarial nets. *Advances in neural information processing systems*, 27, 2014. 1
- [12] Denis A. Gudovskiy, Shun Ishizaka, and Kazuki Kozuka. Cflow-ad: Real-time unsupervised anomaly detection with localization via conditional normalizing flows. *arXiv: Computer Vision and Pattern Recognition*, 2021. 2, 7
- [13] G. E. Hinton and R. R. Salakhutdinov. Reducing the dimensionality of data with neural networks. *Science*, 313(5786):504–507, 2006. 1
- [14] Jonathan Ho, Ajay Jain, and Pieter Abbeel. Denoising diffusion probabilistic models. *neural information processing systems*, 2020. 2
- [15] Jonathan Ho, Ajay Jain, and Pieter Abbeel. Denoising diffusion probabilistic models. In H. Larochelle, M. Ranzato, R. Hadsell, M.F. Balcan, and H. Lin, editors, *Advances in Neural Information Processing Systems*, volume 33, pages 6840–6851. Curran Associates, Inc., 2020. 12
- [16] Jinlei Hou, Yingying Zhang, Qiaoyong Zhong, Di Xie, Shiliang Pu, and Hong Zhou. Divide-and-assemble: Learning block-wise memory for unsupervised anomaly detection. *arXiv: Computer Vision and Pattern Recognition*, 2021. 1, 2
- [17] Chaoqin Huang, Fei Ye, Jinkun Cao, Maosen Li, Ya Zhang, and Cewu Lu. Attribute restoration framework for anomaly detection. *IEEE Transactions on Multimedia*, 2019. 2, 3
- [18] Yann LeCun, Corinna Cortes, and CJ Cui. Mnist handwritten digit database. 2010. 6
- [19] Chun-Liang Li, Kihyuk Sohn, Jinsung Yoon, and Tomas Pfister. Cutpaste: Self-supervised learning for anomaly detection and localization. *arXiv: Computer Vision and Pattern Recognition*, 2021. 1, 7
- [20] Dan Li, Dacheng Chen, Jonathan Goh, and See-kiong Ng. Anomaly Detection with Generative Adversarial Networks for Multivariate Time Series. *arXiv e-prints*, page arXiv:1809.04758, Sept. 2018. 8
- [21] Xiaoyan Li, Iluju Kiringa, Tet Yeap, Xiaodan Zhu, and Yifeng Li. Exploring deep anomaly detection methods based on capsule net. In Cyril Goutte and Xiaodan Zhu, editors, *Advances in Artificial Intelligence*, pages 375–387. Cham, 2020. Springer International Publishing. 8
- [22] Yufei Liang, Jiangning Zhang, Shiwei Zhao, Runze Wu, Yong Liu, and Shuwen Pan. Omni-frequency channel-selection representations for unsupervised anomaly detection. 2022. 7
- [23] Dimitra Maoutsa, Sebastian Reich, and Manfred Opper. Interacting particle solutions of fokker-planck equations through gradient-log-density estimation. *Entropy*, 2020. 3
- [24] Chenlin Meng, Yang Song, Jiaming Song, Jiajun Wu, Jun-Yan Zhu, and Stefano Ermon. Sdedit: Image synthesis and editing with stochastic differential equations. *arXiv: Computer Vision and Pattern Recognition*, 2021. 3
- [25] Pankaj Mishra, Riccardo Verk, Daniele Fornasier, Claudio Picciarelli, and Gian Luca Foresti. Vt-adl: A vision transformer network for image anomaly detection and localization. In *2021 IEEE 30th International Symposium on Industrial Electronics (ISIE)*, pages 01–06, 2021. 6, 7
- [26] Cheng Ouyang, Carlo Biffi, Chen Chen, Turkey Kart, Huaqi Qiu, and Daniel Rueckert. Self-supervision with superpixels: Training few-shot medical image segmentation without annotation. In *European Conference on Computer Vision*, pages 762–780. Springer, 2020. 1
- [27] Pramuditha Perera, Ramesh Nallapati, and Bing Xiang. Ocgan: One-class novelty detection using gans with constrained latent representations. In *Proceedings of the IEEE/CVF Conference on Computer Vision and Pattern Recognition (CVPR)*, June 2019. 8
- [28] Tal Reiss, Niv Cohen, Liron Bergman, and Yedid Hoshen. Panda: Adapting pretrained features for anomaly detection

- and segmentation. In *Proceedings of the IEEE/CVF Conference on Computer Vision and Pattern Recognition*, pages 2806–2814, 2021. [1](#)
- [29] Tal Reiss, Niv Cohen, Liron Bergman, and Yedid Hoshen. Panda: Adapting pretrained features for anomaly detection and segmentation. In *Proceedings of the IEEE/CVF Conference on Computer Vision and Pattern Recognition (CVPR)*, pages 2806–2814, June 2021. [7](#)
- [30] Karsten Roth, Latha Pemula, Joaquin Zepeda, Bernhard Schölkopf, Thomas Brox, and Peter Gehler. Towards total recall in industrial anomaly detection. In *Proceedings of the IEEE/CVF Conference on Computer Vision and Pattern Recognition (CVPR)*, pages 14318–14328, June 2022. [7](#)
- [31] Marco Rudolph, Bastian Wandt, and Bodo Rosenhahn. Same same but different: Semi-supervised defect detection with normalizing flows. *arXiv: Computer Vision and Pattern Recognition*, 2020. [2](#)
- [32] Marco Rudolph, Tom Wehrbein, Bodo Rosenhahn, and Bastian Wandt. Fully convolutional cross-scale-flows for image-based defect detection. 2022. [2](#)
- [33] Lukas Ruff, Robert Vandermeulen, Nico Goernitz, Lucas Deecke, Shoaib Ahmed Siddiqui, Alexander Binder, Emanuel Müller, and Marius Kloft. Deep one-class classification. In Jennifer Dy and Andreas Krause, editors, *Proceedings of the 35th International Conference on Machine Learning*, volume 80 of *Proceedings of Machine Learning Research*, pages 4393–4402. PMLR, 10–15 Jul 2018. [8](#)
- [34] Mohammadreza Salehi, Atrin Arya, Barbod Pajoum, Mohammad Otoofi, Amirreza Shaeiri, Mohammad Hossein Rohban, and Hamid R. Rabiee. Arae: Adversarially robust training of autoencoders improves novelty detection. *Neural Networks*, 144:726–736, 2021. [8](#)
- [35] Mohammadreza Salehi, Niousha Sadjadi, Soroosh Baselizadeh, Mohammad H. Rohban, and Hamid R. Rabiee. Multiresolution knowledge distillation for anomaly detection. In *Proceedings of the IEEE/CVF Conference on Computer Vision and Pattern Recognition (CVPR)*, pages 14902–14912, June 2021. [8](#)
- [36] Thomas Schlegl, Philipp Seeböck, Sebastian M Waldstein, Georg Langs, and Ursula Schmidt-Erfurth. f-anogan: Fast unsupervised anomaly detection with generative adversarial networks. *Medical image analysis*, 54:30–44, 2019. [1](#), [2](#)
- [37] Thomas Schlegl, Philipp Seeböck, Sebastian M Waldstein, Ursula Schmidt-Erfurth, and Georg Langs. Unsupervised anomaly detection with generative adversarial networks to guide marker discovery. In *International conference on information processing in medical imaging*, pages 146–157. Springer, 2017. [1](#)
- [38] Yang Song, Jascha Sohl-Dickstein, Diederik P Kingma, Abhishek Kumar, Stefano Ermon, and Ben Poole. Score-based generative modeling through stochastic differential equations. In *International Conference on Learning Representations*, 2021. [2](#), [3](#), [11](#), [12](#)
- [39] Matthew Tancik, Pratul Srinivasan, Ben Mildenhall, Sara Fridovich-Keil, Nithin Raghavan, Utkarsh Singhal, Ravi Ramamoorthi, Jonathan Barron, and Ren Ng. Fourier features let networks learn high frequency functions in low dimensional domains. In H. Larochelle, M. Ranzato, R. Hadsell, M.F. Balcan, and H. Lin, editors, *Advances in Neural Information Processing Systems*, volume 33, pages 7537–7547. Curran Associates, Inc., 2020. [12](#)
- [40] Hao Tang, Xingwei Liu, Shanlin Sun, Xiangyi Yan, and Xiaohui Xie. Recurrent mask refinement for few-shot medical image segmentation. In *Proceedings of the IEEE/CVF International Conference on Computer Vision*, pages 3918–3928, 2021. [1](#)
- [41] Pascal Vincent. A connection between score matching and denoising autoencoders. *Neural Computation*, 2011. [3](#)
- [42] Guodong Wang, Shumin Han, Errui Ding, and Di Huang. Student-teacher feature pyramid matching for anomaly detection. *arXiv preprint arXiv:2103.04257*, 2021. [5](#)
- [43] Zhou Wang, Alan C Bovik, Hamid R Sheikh, and Eero P Simoncelli. Image quality assessment: from error visibility to structural similarity. *IEEE transactions on image processing*, 13(4):600–612, 2004. [2](#)
- [44] Julia Wolleb, Florentin Bieder, Robin Sandkühler, and Philippe C. Cattin. Diffusion Models for Medical Anomaly Detection. *arXiv e-prints*, page arXiv:2203.04306, Mar. 2022. [8](#)
- [45] Julian Wyatt, Adam Leach, Sebastian M. Schmon, and Chris G. Willcocks. Anodpdm: Anomaly detection with denoising diffusion probabilistic models using simplex noise. In *Proceedings of the IEEE/CVF Conference on Computer Vision and Pattern Recognition (CVPR) Workshops*, pages 650–656, June 2022. [8](#)
- [46] Shinji Yamada and Kazuhiro Hotta. Reconstruction student with attention for student-teacher pyramid matching. *arXiv preprint arXiv:2111.15376*, 2021. [5](#)
- [47] Jie Yang, Yong Shi, and Zhiquan Qi. Dfr: Deep feature reconstruction for unsupervised anomaly segmentation. *arXiv: Computer Vision and Pattern Recognition*, 2020. [5](#)
- [48] Jongmin Yoon, Sung Ju Hwang, and Juho Lee. Adversarial purification with score-based generative models. *arXiv: Learning*, 2021. [3](#)
- [49] Jiawei Yu1, Ye Zheng, Xiang Wang, Wei Li, Yushuang Wu, Rui Zhao, and Liwei Wu1. Fastflow: Unsupervised anomaly detection and localization via 2d normalizing flows. 2022. [2](#), [7](#)
- [50] Vitjan Zavrtanik, Matej Kristan, and Danijel Skočaj. Draem - a discriminatively trained reconstruction embedding for surface anomaly detection. In *Proceedings of the IEEE/CVF International Conference on Computer Vision (ICCV)*, pages 8330–8339, October 2021. [1](#), [2](#), [7](#)
- [51] Vitjan Zavrtanik, Matej Kristan, and Danijel Skočaj. Reconstruction by inpainting for visual anomaly detection. *Pattern Recognition*, 112:107706, 2021. [2](#), [7](#)

## A. Supplementary formula

### A.1. Proof for the true trajectory

First, we define the true trajectory from  $\mathbf{x}(t)$  to  $\mathbf{x}(0)$  in the sense that after obtaining  $\mathbf{x}(t)$  by injecting noise into  $\mathbf{x}(0)$ , the path is iterated back to the original  $\mathbf{x}(0)$  through reverse stochastic process. The proof of the key formulation about the true trajectory from  $\mathbf{x}(t)$  to  $\mathbf{x}(0)$  is given below.

The objective of a generative model is to generate samples that satisfy the distribution of the given training data. Recalling Section 3.1, we train a neural network to fit the score function:  $\nabla_{\mathbf{x}} \log p_t(\mathbf{x}(t))$  of given dataset  $\mathbf{X}_N$ , which guarantees the score-based generative model eventually generate  $\mathbf{x}(0) \sim p_0(\mathbf{x})$  through reverse process, where  $p_0(\mathbf{x}) \approx p_{data}(\mathbf{x})$  by definition. Here,

$$\begin{aligned}
\frac{\partial \log p_t(\mathbf{x}(t))}{\partial \mathbf{x}(t)} &= \frac{1}{p_t(\mathbf{x}(t))} \frac{\partial p_t(\mathbf{x}(t))}{\partial \mathbf{x}(t)} \\
&= \frac{1}{p_t(\mathbf{x}(t))} \frac{\partial}{\partial \mathbf{x}(t)} \int p_0(\mathbf{x}(0)) p_{0t}(\mathbf{x}(t)|\mathbf{x}(0)) d\mathbf{x}(0) \\
&= \frac{1}{p_t(\mathbf{x}(t))} \int p_0(\mathbf{x}(0)) \frac{\partial p_{0t}(\mathbf{x}(t)|\mathbf{x}(0))}{\partial \mathbf{x}(t)} d\mathbf{x}(0) \\
&= \frac{1}{p_t(\mathbf{x}(t))} \int p_0(\mathbf{x}(0)) p_{0t}(\mathbf{x}(t)|\mathbf{x}(0)) \frac{\partial \log p_{0t}(\mathbf{x}(t)|\mathbf{x}(0))}{\partial \mathbf{x}(t)} d\mathbf{x}(0) \\
&= \int \frac{p_0(\mathbf{x}(0)) p_{0t}(\mathbf{x}(t)|\mathbf{x}(0))}{p_t(\mathbf{x}(t))} \frac{\partial \log p_{0t}(\mathbf{x}(t)|\mathbf{x}(0))}{\partial \mathbf{x}(t)} d\mathbf{x}(0).
\end{aligned} \tag{6}$$

However, regarding the true trajectory from  $\mathbf{x}(t)$  to  $\mathbf{x}(0)$ , we can consider that  $p_{data}(\mathbf{x})$  degenerates to a one-point distribution with mean  $\mathbf{x}(0)$  and variance 0, denoted as  $p''_{data}(\mathbf{x})$ :

$$p''_{data}(\mathbf{x}) = \begin{cases} 1, & \mathbf{x} = \mathbf{x}(0) \\ 0, & \text{Others} \end{cases} \tag{7}$$

Therefore,  $\nabla_{\mathbf{x}} \log p''_t(\mathbf{x}(t)) = \nabla_{\mathbf{x}} \log p''_{0t}(\mathbf{x}(t)|\mathbf{x}(0))$ . As discussed in Section 3.1, if the drift coefficient  $f(t)$  of the SDE is linear, the transition density is Gaussian  $p_{0t}(\mathbf{x}(t)|\mathbf{x}(0)) = \mathcal{N}(\mathbf{x}(t); \mu(t)\mathbf{x}(0), \sigma(t)^2 \mathbf{I})$ . Thus,  $\nabla_{\mathbf{x}} \log p''_t(\mathbf{x}(t)) = -\frac{\mathbf{x}(t) - \mu(t)\mathbf{x}(0)}{\sigma(t)^2} = -\frac{\mathbf{z}(t)}{\sigma(t)}$ , where  $\mathbf{x}(t) = \mu(t)\mathbf{x}(0) + \sigma(t)\mathbf{z}(t)$ ,  $\mathbf{z}(t) \sim \mathcal{N}(0, \mathbf{I})$ , denoted as self-score  $s_e(\cdot, t)$  in our paper. Therefore, we can obtain Eq.(6) and Eq.(7) by plugging  $\nabla_{\mathbf{x}} \log p''_t(\mathbf{x}(t))$  into Eq.(2) and Eq.(5) respectively.

$$d\mathbf{x}(t) = (f(t)\mathbf{x}(t) - g(t)^2 \left(-\frac{\mathbf{z}(t)}{\sigma(t)}\right)) d\bar{t} + g(t) d\bar{\mathbf{w}}(t). \tag{8}$$

$$d\mathbf{x}(t) = (f(t)\mathbf{x}(t) - \frac{1}{2}g(t)^2 \left(-\frac{\mathbf{z}(t)}{\sigma(t)}\right)) dt. \tag{9}$$

The path obtained by iterating Eq. (8) is represented as the true trajectory from  $\mathbf{x}(t)$  to  $\mathbf{x}(0)$  with the Reverse SDE in Eq.(2), and the path from Eq. (9) as the true trajectory with the probability flow ODE in Eq.(5). In addition, when training the score-based model, whole-score is actually evaluated through self-score  $-\frac{\mathbf{z}(t)}{\sigma(t)}$  of each sample in the training dataset. And we can provide more insights of the principle of **score-AD** by analyzing the difference of whole-score and self-score in calculation ways with Eq. (6).

### A.2. Details VE, VP and sub-VP SDEs

We follow the definitions of VE, VP and sub-VP SDEs as in [38], and show them in order:

$$\begin{cases} d\mathbf{x}(t) = \sqrt{\frac{d[\sigma^2(t)]}{dt}} d\mathbf{w}(t), \\ d\mathbf{x}(t) = -\frac{1}{2}\beta(t)\mathbf{x}(t)dt + \sqrt{\beta(t)}d\mathbf{w}(t), \\ d\mathbf{x}(t) = -\frac{1}{2}\beta(t)\mathbf{x}(t)dt + \sqrt{\beta(t)}(1 - e^{-2\int_0^t \beta(s)ds})d\mathbf{w}(t). \end{cases} \tag{10}$$

VE SDE refers to Variance Exploding (VE) SDE because VE SDE always gives a process with exploding variance when  $t$  increases. The Variance Preserving (VP) SDE yields a process with a fixed variance of one when the initial distribution has unit variance. The variance of the stochastic process induced by the sub-VP SDE is always bounded by the VP SDE at every intermediate time step. See [38] for more information.

Because VE, VP and sub-VP SDEs all have linear drift coefficients  $f(t)$ , their corresponding transition densities  $p_{0t}(\mathbf{x}(t)|\mathbf{x}(0))$  are all Gaussian:

$$\begin{cases} \mathcal{N}(\mathbf{x}(t); \mathbf{x}(0), [\sigma^2(t) - \sigma^2(0)]\mathbf{I}) & \text{(VE SDE)} \\ \mathcal{N}(\mathbf{x}(t); \mathbf{x}(0) e^{-\frac{1}{2}\int_0^t \beta(s)ds}, \mathbf{I} - \mathbf{I} e^{-\int_0^t \beta(s)ds}) & \text{(VP SDE)} \\ \mathcal{N}(\mathbf{x}(t); \mathbf{x}(0) e^{-\frac{1}{2}\int_0^t \beta(s)ds}, [1 - e^{-\int_0^t \beta(s)ds}]^2 \mathbf{I}) & \text{(sub-VP SDE)} \end{cases} \tag{11}$$

In detail, there are discretizations of SDEs. For VE SDE, set

$$\sigma(t) = \begin{cases} \sigma_{\min} \left(\frac{\sigma_{\max}}{\sigma_{\min}}\right)^t, & t \in (0, 1] \\ 0, & t = 0. \end{cases} \tag{12}$$

For both VP SDE and sub-VP SDE, they are set as:

$$\beta(t) = \beta_{\min} + t(\beta_{\max} - \beta_{\min}). \tag{13}$$

### A.3. Algorithm

From Eq. (8) and Eq. (9), we can approach the original  $\mathbf{x}(0)$  from  $\mathbf{x}(t)$  if we know  $\mathbf{z}(t)$  relative to  $\mathbf{x}(0)$  at each moment. It should be noted that the  $\mathbf{z}(t_i)$  changes constantly over steps, and by deforming Eq.(4),  $\mathbf{z}(t) = \frac{\mathbf{x}(t) - \mu(t)\mathbf{x}(0)}{\sigma(t)}$ , we can know it will be updated along with  $\mathbf{x}''(t_i)$ . At the current step, as the  $\mathbf{z}(t_i)$  is known in advance, we can bring

---

**Algorithm 1** Score-AD with the flow ODE

---

**Require:**  $\mathbf{x}(0); \{t\}; r;$ 

- 1: **for**  $t \in \{t\}$  **do**
- 2:    $\mathbf{x}(t) = \mu(t)\mathbf{x}(0)$
- 3:    $\mathbf{z}(t) \sim \mathcal{N}(0, I)$
- 4:    $\mathbf{x}(t_0) = \mathbf{x}(t) + \sigma(t)\mathbf{z}(t)$
- 5:   **for**  $i = 0$  **to**  $r - 1$  **do**

$$\Delta t = t_i - t_{i+1}$$

$$\mathbf{x}'(t_{i+1}) = \mathbf{x}'(t_i) - f(t_i)\mathbf{x}'(t_i)\Delta t$$

$$\mathbf{x}'(t_{i+1}) = \mathbf{x}'(t_{i+1}) + \frac{1}{2}g(t_i)^2 s_\theta(\mathbf{x}', t_i)\Delta t$$

- 6:    $\mathbf{x}''(t_{i+1}) = \mathbf{x}''(t_i) - f(t_i)\mathbf{x}''(t_i)\Delta t$

$$\mathbf{x}''(t_{i+1}) = \mathbf{x}''(t_{i+1}) + \frac{1}{2}g(t_i)^2 \left(-\frac{\mathbf{z}(t_i)}{\sigma(t_i)}\right)\Delta t$$

$$\mathbf{z}(t_{i+1}) = \frac{\mathbf{x}''(t_{i+1}) - \mu(t_{i+1})\mathbf{x}(0)}{\sigma(t_{i+1})}$$

- 7:   **end for**
  - 8:   Input  $\mathbf{x}'(t_r)$  and  $\mathbf{x}''(t_r)$  to the score model
  - 9: **end for**
  - 10: Add or multiply feature maps
  - 11: **return** Anomaly Map
- 

---

**Algorithm 2** Score-AD with Reverse SDE

---

**Require:**  $\mathbf{x}(0); \{t\}; r;$ **for**  $t \in \{t\}$  **do**

- 2:    $\mathbf{x}(t) = \mu(t)\mathbf{x}(0)$
- 3:    $\mathbf{z}(t) \sim \mathcal{N}(0, I)$
- 4:    $\mathbf{x}(t_0) = \mathbf{x}(t) + \sigma(t)\mathbf{z}(t)$
- 5:   **for**  $i = 0$  **to**  $r - 1$  **do**

$$\Delta t = t_i - t_{i+1}$$

$$\mathbf{n}(t_i) \sim \mathcal{N}(0, I)$$

$$\mathbf{x}'(t_{i+1}) = \mathbf{x}'(t_i) - f(t_i)\mathbf{x}'(t_i)\Delta t$$

$$\mathbf{x}'(t_{i+1}) = \mathbf{x}'(t_{i+1}) + g(t_i)^2 s_\theta(\mathbf{x}', t_i)\Delta t$$

$$\mathbf{x}'(t_{i+1}) = \mathbf{x}'(t_{i+1}) + g(t_i)\sqrt{\Delta t}\mathbf{n}(t_i)$$

- 6:    $\mathbf{x}''(t_{i+1}) = \mathbf{x}''(t_i) - f(t_i)\mathbf{x}''(t_i)\Delta t$

$$\mathbf{x}''(t_{i+1}) = \mathbf{x}''(t_{i+1}) + g(t_i)^2 \left(-\frac{\mathbf{z}(t_i)}{\sigma(t_i)}\right)\Delta t$$

$$\mathbf{x}''(t_{i+1}) = \mathbf{x}''(t_{i+1}) + g(t_i)\sqrt{\Delta t}\mathbf{n}(t_i)$$

$$\mathbf{z}(t_{i+1}) = \frac{\mathbf{x}''(t_{i+1}) - \mu(t_{i+1})\mathbf{x}(0)}{\sigma(t_{i+1})}$$

**end for**

- 8:   Input  $\mathbf{x}'(t_r)$  and  $\mathbf{x}''(t_r)$  to the score model
  - 9: **end for**
  - 10: Add or multiply feature maps
  - 11: **return** Anomaly Map
- 

self-score computed by  $\mathbf{z}(t_i)$  to Eq. (8) or Eq. (9) to obtain  $\mathbf{x}''(t_{i+1})$ . Through above deformation of Eq.(4) and  $\mathbf{x}''(t_{i+1})$ , we can therefore obtain  $\mathbf{z}(t_{i+1})$ . Repeating this process, we can obtain the complete trajectory of  $\mathbf{x}(t)$  to  $\mathbf{x}''(t_r)$ , or ultimately to  $\mathbf{x}''(0) \approx \mathbf{x}(0)$ . Therefore, after  $r$  steps, we can feed the sets  $\{\mathbf{x}'(t_r)\}$  and  $\{\mathbf{x}''(t_r)\}$  (each of which has a capacity of  $T$ ) into the score-based model. We conclude the algorithm about **Score-AD**. Algorithms 1 and 2 denote the reverse diffusion process with the probability flow ODE and Reverse SDE separately.  $\mathbf{x}(0) \in \mathbf{X}_{N+A}$  is a test image,  $\{t\}$  is a set of different initial times with capacity of  $T$ , and  $r$  is the number of iteration steps.

## B. Implementation Details

Below, we add additional implementation details for each experiment.

**MNIST Figure.** For Fig. 1, to demonstrate our method and show more insights, we train a score model on a subset with category “1” on the MNIST dataset while selecting an image with category “7” for testing. The score model is based on VE SDE, which adopts the U-net architecture and code can be found in the COLAB tutorial of [https://github.com/yang-song/score\\_sde\\_pytorch](https://github.com/yang-song/score_sde_pytorch). We choose  $\sigma(t) = (25)^t$ , set diffusion timesteps as 1000 and initial moment  $t = 0.2$  to get the final reconstructed image.

**MNIST Experiment.** We choose VP SDE. Specially,

$\beta_{min} = 0.1$ ,  $\beta_{max} = 20$ , and set diffusion timesteps as 1000. Based on the previous work, we adopt the positional embeddings, the layers in [15] to condition the score model on continuous time variables. As for architecture of score-based model, we take DDPM++ structure introduced in [38]: **1**) rescales skip connections; **3**) employs BigGAN-type residual blocks; **4**) uses 2 residual blocks per resolution; and **5**) uses “residual” for input. Please see [38] and [yang-song/score\\_sde\\_pytorch](https://github.com/yang-song/score_sde_pytorch) to get more information.

**Exploratory experiment.** For Fig. 3, based on the instantiation scheme of VE SDE, we choose  $\sigma_{min} = 0.1$  and  $\sigma_{max} = 20$ . Specially, we select three data points  $(-6.0, 5.0)$ ,  $(5.17, 5.2)$ ,  $(-4.2, -4.3)$ . Based on our assumption and normal data distribution,  $(-6.0, 5.0)$  is anomaly data. Consistent with the results in Fig. 3, the difference in whole-score value between the “reconstructed and original noisy” data pairs is much larger than for normal data.

**MvTec AD and BeanTech AD dataset.** The MvTec AD dataset is available at <https://www.mvtec.com/company/research/datasets/mvtec-ad/> and the BTAD dataset is available at <https://github.com/pankajmishra000/VT-ADL>. For VE SDE, we choose  $\sigma_{min} = 0.01$  and  $\sigma_{max} = 348$ . For VP SDE and sub-VP SDE, we select  $\beta_{min} = 0.1$  and  $\beta_{max} = 20$ . Based on the previous work, we use random Fourier feature embeddings layers introduced in [39] to condition the score

model on continuous time variables for VE SDE, and the scale parameter of Fourier feature embeddings is fixed at 16. For VP and sub-VP SDE, we adopt positional embeddings. As for the architecture of a score-based model, we take the NCSN++ structure for all SDEs : **1)** uses FIR upsampling/downsampling; **2)** rescales skip connections; **3)** employs BigGAN-type residual blocks; **4)** uses 2 residual blocks per resolution; and **5)** uses "residual" for input and no progressive growing architecture for output. The code for the score-based model can be found at [yang-song/score\\_sde\\_pytorch](https://github.com/yang-song/score_sde_pytorch). The results of Tab. 2 are based on VPSDE and Flow ODE sampling methods. For the results of Tab. 1, to choose a set of different initial moment  $\{t\}$ , we adjust the maximum and minimum  $t$  in  $\{t\}$ , and then take time stamp every 50 steps interval. The selected feature maps, or  $\{t\}$  set, work well and are effective in most cases, but not on every image. Therefore, an adaptive feature map selection strategy would be helpful and could be our future extension.